AIAA JOURNAL
Vol. 40, No. 9, September 2002

Higher Mean-Flow Approximation for Solid Rocket Motors with Radially Regressing Walls

Joseph Majdalani* and Anand B. Vyas†
Marquette University, Milwaukee, Wisconsin 53233
and
Gary A. Flandro‡
University of Tennessee Space Institute, Tullahoma, Tennessee 37388

The bulk gas motion in a circular-port rocket motor is described using a rotational, incompressible, and viscous flow model that incorporates the effect of wall regression. The mathematical idealization developed is also applicable to semi-open porous tubes with expanding walls. Based on mass conservation, a linear variation in the mean axial velocity is ascertained. This relationship suggests investigating a spatial transformation of the Proudman–Johnson form. With the use of similar arguments, a temporal transformation is also introduced. When these transformations are applied in both space and time, the Navier–Stokes equations are reduced to a single, nonlinear, fourth-order differential equation. Following this exact Navier–Stokes reduction, the resulting problem is solved using variation of parameters and small-parameter perturbations. The asymptotic solutions for the velocity, pressure, vorticity, and shear are obtained as function of the injection Reynolds number *Re* and the dimensionless regression ratio α. By way of verification, it is shown that, as $\alpha/Re \to 0$, Yuan and Finkelstein's solutions can be restored from ours. Similarly, as $\alpha/Re \to 0$, Culick's inviscid profile is recovered. It is demonstrated that, for a range of small α/Re, inviscid solutions are practical. However, for fast burning propellants under development, the inviscid assumption deteriorates. Because it is applicable over a broader range of operating parameters, the current analysis leads to a closed-form mean-flow solution that can be used, instead of the inviscid profile, to 1) prescribe an adjusted aeroacoustic field, 2) describe the so-called acoustic boundary layer, 3) evaluate the viscous and rotational contributions to the acoustic stability growth rate factor, 4) track the evolution of hydrodynamic instability, and 5) accurately simulate the internal gasdynamics in rapidly regressing motors and cold-flow experiments with medium-to-high levels of injection.

Nomenclature

A	=	permeance; in live propellants, $\rho_s/\rho - 1$
$A_b(\bar{z})$	=	porous boundary or burning surface area, $2\pi a\bar{z}$
A_c	=	cross-sectional area, πa^2
a	=	instantaneous wall radius, m
$\dot{a}$	=	wall regression rate, m/s
F	=	similarity function, $\bar{F}/Re$
$\bar{p}$	=	dimensional pressure, Pa
Re	=	injection Reynolds number
r	=	normalized radial coordinate, $\bar{r}/a$
$\bar{r}$	=	radius, m
t	=	time, s
$\bar{u}$	=	velocity $(\bar{u}_r, \bar{u}_z)$, m/s
z	=	normalized axial coordinate, $\bar{z}/a$
$\bar{z}$	=	axial coordinate, m
α	=	dimensionless regression ratio
Δ	=	difference
ε	=	reciprocal of the injection Reynolds number
η	=	transformed radial coordinate, $\frac{1}{2}r^2$
θ	=	recurring coordinate, $\frac{1}{2}\pi r^2$
ϑ	=	control volume
ν	=	kinematic viscosity, m^2/s
ρ	=	density, kg/m^3
τ	=	normalized shear stress
ψ	=	normalized stream function
Ω	=	normalized vorticity

Subscripts

b	=	porous boundary or burning surface
c	=	cross section
m	=	spatial mean value at a given cross section
r, z	=	radial or axial component; term used for derivatives
s	=	solid phase
t	=	temporal derivative

Presented as Paper 2001-3870 at the AIAA/ASME/SAE/ASEE 37th Joint Propulsion Conference, Salt Lake City, UT, 8–11 July 2001; received 23 August 2001; revision received 15 February 2002; accepted for publication 20 February 2002.

*Assistant Professor, Department of Mechanical and Industrial Engineering; Joseph.Majdalani@Marquette.edu. Member AIAA.

†Graduate Student and Research Associate, Department of Mechanical and Industrial Engineering; Anand.Vyas@Marquette.edu. Student Member AIAA.

‡Boling Chair Professor of Mechanical and Aerospace Engineering; gflandro@utsi.edu. Associate Fellow AIAA.

I. Introduction

NUMEROUS studies have addressed the motion of an injection-driven fluid inside a tube with transpiring walls. Past and recent interests have covered a broad spectrum of technical applications. These include paper making,[1] sweat cooling,[2,3] flow filtration,[4–6] boundary-layer control,[7–9] and internal flow modeling in solid rocket motors. Ongoing interest is evidenced by the rigorous mathematical analyses carried out recently by Banks and Zaturska,[10] Zaturska and Banks,[11] Cox and King,[12] King and Cox,[13] and Lu.[14,15] Internal flow modeling has received considerable attention due to the central role that it occupies in the assessment of aeroacoustic instabilities in rockets.[16–18] In part, this is due to the strong dependence of stability integrals on the precise determination of velocity and pressure fields. The daunting task of describing the gasdynamics inside rocket motors has, hence, motivated, over the last four decades, the quest for several mathematical idealizations of increasing level of refinement.

To better understand the evolution of the problem at hand, note that the internal flow has been traditionally viewed as consisting of a superposition of mean and unsteady fields. Also note that the unsteady field is largely prescribed by the mean-flow motion. In

view of this intimate coupling, one is justified in seeking both flow components under the same flow conditions and using comparable orders of accuracy.

The first adequate mean-flow approximation was presented by Culick[19] in 1966. This constituted a visible improvement over the one-dimensional solution used in previous studies.[20] Despite its neglect of small viscous effects, Culick's steady and incompressible profile[19] was rotational; it could satisfy the fundamental boundary conditions associated with an idealized rocket motor. Unlike its predecessor,[20] it could now fulfill the no-slip restriction at the wall by ensuring that gases enter the chamber perpendicularly to the burning surface. Because it is inviscid, Culick's profile[19] was exact in the limit of an infinitely large injection Reynolds number *Re*. Overall, it was convenient, simple, and reasonably accurate over a practical range of Reynolds numbers exceeding 1000. It also lent itself to both numerical[21] and experimental verifications by Dunlap et al.[22] and Yamada et al.[23] Aside from a small region near the head end of the chamber, Culick's profile[19] appeared to approximate closely the values measured in a porous tube with real gas. This gave Varapaev and Yagodkin[24] the impetus to use it as the basis for their investigation of hydrodynamic instability. In the same context, it has been recently employed by Casalis et al.[25] and Griffond et al.[26] to investigate the evolution of turbulence in both planar[25] and axisymmetric configurations.[26] Whereas Varapaev and Yagodkin[24] have undertaken a preliminary study of the linear stability of Culick's profile,[19] Casalis et al.[25] and Griffond et al.[26] have employed a modern approach from which results could be used to predict experimentally measured turbulence. These efforts have suggested the presence of a hydrodynamic source of instability that has not yet been accounted for in combustion stability theory. A similar conclusion has been reached by Flandro and Majdalani,[18] who have attributed the discrepancy to one-dimensional limitations undermining the standard formulation in use today.[27,28] When a one-dimensional representation is adopted to describe the unsteady field, two- and three-dimensional interactions are inadvertently precluded. Several sources of instability are consequently suppressed, including turbulent energy. This inherent restriction explains the inability of the traditional formulation to physically account for flow turning and other vorticity-driven phenomena. Several corroborative studies are now available, for example, in which the onset of turbulence in porous-walled channels or tubes is confirmed to be a source of instability. To name a few, one may cite Lee and Beddini,[29,30] Beddini and Roberts,[31] Sabnis et al.,[32] Tissier et al.,[33] Roh et al.,[34] and Apte and Yang.[35] Others in which vortex-driven phenomena have emerged include studies of the parietal vortex shedding that has been identified to be a source of instability that eludes traditional theory.[36–40] Naturally, the production and propagation of so-called crawling vortices is strongly influenced by the mean-flow motion.[37] In addition to its pertinence to studies of hydrodynamic instability, the mean-flow profile has also been influential in the development of unsteady flow dynamics used to describe the aeroacoustic wave motion inside rocket motors.[41–45]

In Flandro's[41] continued attempts to point out the shortcomings of using one-dimensional plane wave solutions,[46] he pursued multidimensional formulations for the unsteady core flow.[41] Initially, Flandro presented a simple analytical solution for the oscillatory field that accounted for the presence of solid boundaries.[42] His early model was two dimensional only artificially because it ignored the downstream convection of unsteady vorticity together with the spatial depreciation of Culick's radial velocity.[19] It was, however, valid in a small region above the burning surface, where most significant interactions evolved. An asymptotic solution by Majdalani and Van Moorhem followed.[43,44] The latter employed the exact Culick profile[19] but ignored the axial dependency.

Flandro[16] later presented an inviscid solution that faithfully retained Culick's profile[19] and the correct spatial dependency. Shortly thereafter, Flandro produced a multidimensional solution that retained viscous effects.[17] A practically equivalent solution based on multiple scales was independently arrived at by Majdalani and Van Moorhem.[43] Majdalani and Van Moorhem[45] would later demonstrate the agreement between both contemporaneous solutions and full numerical simulations. Their results were also found to agree with test measurements acquired by Barron et al.,[47] Brown et al.,[48] and Dunlap et al.[49] The multiple-scale solution was also capable of elucidating the acoustic boundary layer, which until then had been the subject of much controversy.[50]

The Cartesian slab-rocket geometry has also been analyzed by Majdalani and Roh[51] and, for an arbitrary mean-flow profile, by Majdalani[52] and Majdalani and Van Moorhem.[53] Pursuant to these studies, a fully rotational and viscous representation of the aeroacoustic field has been established. Besides being of higher order, the newly developed expressions by Majdalani,[52] Majdalani and Van Moorhem,[53] and Majdalani and Flandro[54] have offered the advantage of accommodating any conceivable mean-flow profile. Because the level of precision achieved in these recent studies is limited by the accuracy of the mean-flow solution, the need arises today for an improved mean-flow approximation that is consistent with the unsteady flow details.

In addition to that, a more comprehensive mean-flow solution can 1) improve the accuracy of time-dependent models, 2) provide a better platform to investigate hydrodynamic stability, and 3) enhance our flow predictive capabilities; it also serves to extend the range over which current models apply. In fact, according to Yuan[55] (cf., p. 267), there are numerous problems of real interest that exhibit injection Reynolds numbers in the 10–1000 range. One such example corresponds to a recent core-flow simulation carried out at the Center for Simulation of Advanced Rockets (CSAR), where an injection Reynolds number of 47.6 was held constant throughout the numerical study.[56]

For the foregoing reasons, it is the purpose of this paper to obtain a mean-flow solution that not only satisfies the basic boundary conditions, but is also capable of incorporating viscous forces and wall regression. A direct consequence of such an effort will be the attainment of an internal flow approximation that is consistently rotational and viscous in both its mean and oscillatory components. Furthermore, it is anticipated that the higher-order approximation will be useful over a broader range of operating parameters, including the 10–1000 range. In actuality, the need for a higher approximation has been alluded to in recent studies by Lee and Beddini[29,30] and Apte and Yang.[57] In the former study,[29,30] retention of the Reynolds number was found to be important due to the impact of viscous dissipation on the acoustic boundary layer at constant frequency. In the latter study,[57] a numerical simulation of a nozzleless rocket motor was carried out in which Taylor's inviscid representation was found to be inadequate for $Re < 500$ (Ref. 57, pp. 807, 808). The search for a higher approximation is further motivated by the need to model motors with fast burning propellants, namely, those being developed for high-acceleration interceptor vehicles. In that context, it may be argued that the availability of a closed-form solution can be instrumental in validating numerical simulations of the regression process (private communication, R. A. Fiedler, CSAR, University of Illinois at Urbana–Champaign, 2001). Aside from the foregoing reasons, note that this work serves to extend the planar solution presented recently by Zhou and Majdalani.[58]

In principle, the paper can be divided into two parts. In the first, Goto and Uchida's approach[59] is applied to reduce the Navier–Stokes system into a single Proudman–Johnson equation.[60] The procedure involves a spatial transformation that presumes a linearly varying axial velocity and a temporal transformation that is granted by a time-invariant dimensionless regression. In the second part, we follow Yuan and Finkelstein[61] and Terrill and Thomas[21] in perturbing the resulting nonlinear equation. In the process, we find it necessary to apply the method of variation of parameters in a quadruple fashion. At length, a higher-order mean-flow approximation is obtained for the velocity, pressure, vorticity, and shear stress distributions. These flow attributes are described in addition to limiting process verifications that are occasionally resorted to. Our results clearly indicate the existence of a range over which the inviscid approximation deteriorates. Conversely, the suitability of Culick's profile[19,46] is demonstrated over a substantial range of conditions characterizing solid rocket motors. A numerical comparison that is identical to that described by Zhou and Majdalani[58] is also carried out; it will be omitted here in the interest of brevity.

II. Mathematical Model

The internal-burning cylindrical grain of a solid rocket motor is idealized as a long tube with one end closed. The tube's circumferential walls are assumed to be sufficiently permeable to allow the radial inflow of a secondary fluid. The incoming stream turns and merges into the primary axial flow. The forthcoming analysis is general enough to accommodate both liquid and gaseous injectants. As the circumferential walls expand at a speed equal to $\dot{a}$, the head end is assumed to be sufficiently compliant to stretch in the radial direction while remaining perpendicular to the tube's axis. As shown in Fig. 1a, a coordinate system can be chosen based on axisymmetry. With this choice, the incompressible mass and momentum conservation equations may be written as

$$\frac{\partial(\bar{r}\bar{u}_z)}{\partial\bar{z}} + \frac{\partial(\bar{r}\bar{u}_r)}{\partial\bar{r}} = 0 \tag{1}$$

$$\frac{\partial\bar{u}_z}{\partial t} + \bar{u}_z\frac{\partial\bar{u}_z}{\partial\bar{z}} + \bar{u}_r\frac{\partial\bar{u}_z}{\partial\bar{r}} = -\frac{1}{\rho}\frac{\partial\bar{p}}{\partial\bar{z}} + \nu\left[\frac{\partial^2\bar{u}_z}{\partial\bar{z}^2} + \frac{1}{\bar{r}}\frac{\partial}{\partial\bar{r}}\left(\bar{r}\frac{\partial\bar{u}_z}{\partial\bar{r}}\right)\right] \tag{2}$$

$$\frac{\partial\bar{u}_r}{\partial t} + \bar{u}_z\frac{\partial\bar{u}_r}{\partial\bar{z}} + \bar{u}_r\frac{\partial\bar{u}_r}{\partial\bar{r}} = -\frac{1}{\rho}\frac{\partial\bar{p}}{\partial\bar{r}} + \nu\left[\frac{\partial^2\bar{u}_r}{\partial\bar{z}^2} + \frac{\partial}{\partial\bar{r}}\left(\frac{1}{\bar{r}}\frac{\partial(\bar{r}\bar{u}_r)}{\partial\bar{r}}\right)\right] \tag{3}$$

where variables have their usual significance or as given in the Nomenclature. Boundary conditions are

$$\bar{r} = a(t), \qquad \bar{u}_z = 0, \qquad \bar{u}_r = -V$$
$$\bar{r} = 0, \qquad \frac{\partial\bar{u}_z}{\partial r} = 0, \qquad \bar{u}_r = 0$$
$$\bar{z} = 0, \qquad \bar{u}_z = 0 \tag{4}$$

and V is the absolute velocity at the wall. These conditions allow for a time-dependent radius at $\bar{r} = a(t)$, where the porous wall is located. Along this surface, the no-slip mechanism dictates a zero axial velocity, $\bar{u}_z = 0$, and a radial influx according to $\bar{u}_r = -V$. Along the centerline, $\bar{r} = 0$, symmetry is reflected in both $\partial\bar{u}_z/\partial r = 0$ and $\bar{u}_r = 0$. The final boundary condition applies to the head end, $\bar{z} = 0$, where the infinite impedance requires setting $\bar{u}_z = 0$.

A. Basic Assumptions

Equations (1–4) are written under the following implicit assumptions:

1) The bulk flow is incompressible and isothermal.
2) Body forces are absent.

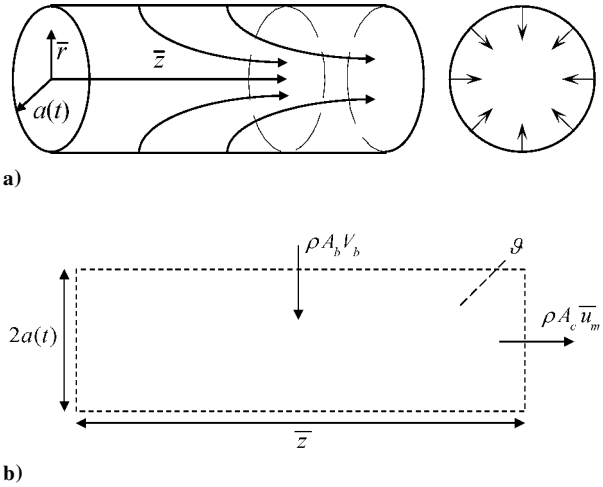

Fig. 1 Schematic of a cylindrical motor showing a) coordinate system used to capture wall regression and b) control volume used in the mass balance calculation.

3) The kinematic viscosity ν is constant.
4) The fluid enters the tube at a spatially uniform velocity $V(t)$.
5) Swirling effects are ignored.
6) The azimuthal component of velocity is zero.
7) Laminar conditions are prevalent.
8) No heat is transferred to the gas.

B. General Mass Balance Requirement

Consider in Fig. 1b a control volume ϑ extending from the head end to an arbitrary position $\bar{z}$. The average axial flow velocity $\bar{u}_m(\bar{z}, t)$ at a given cross section $A_c = \pi a^2$ can be determined from

$$\bar{u}_m(\bar{z}, t) = \frac{1}{A_c}\int_{A_c}\bar{\boldsymbol{u}}(\bar{z}, \bar{r}, t)\cdot \mathrm{d}\boldsymbol{A} \tag{5}$$

where $\bar{\boldsymbol{u}}$ is the local axial velocity and $\mathrm{d}\boldsymbol{A} = \boldsymbol{k}\,\mathrm{d}A$ is the differential surface-area vector. When $A_b(\bar{z}) = 2\pi a\bar{z}$ is used to denote the volume's circumferential area, conservation of mass across ϑ requires that

$$\frac{\partial}{\partial t}\int_{\vartheta}\rho\,\mathrm{d}\vartheta + \int_{A_c}\rho\bar{\boldsymbol{u}}\cdot\mathrm{d}\boldsymbol{A} - \rho A_b V_b = 0 \tag{6}$$

where $\mathrm{d}\vartheta = \pi a^2\bar{z}$ and V_b is the fluid velocity with respect to the wall. Recalling that the flow is incompressible, one may substitute Eq. (5) into Eq. (6) and integrate from 0 to $\bar{z}$. One obtains

$$\bar{u}_m = \frac{A_b}{A_c}V_b - \frac{\bar{z}}{A_c}\frac{\partial A_c}{\partial t} = 2\frac{\bar{z}}{a}(V_b - \dot{a}) = 2\frac{\bar{z}}{a}V \tag{7}$$

where $V = V_b - \dot{a}$ is the absolute inflow velocity with respect to an inertial reference frame. Equation (7) indicates that the mean velocity is linearly proportional to the axial coordinate. Because integration in Eq. (5) does not affect $\bar{z}$, this axial dependence in $\bar{u}_m$ can only be realized when $\bar{u}_z(\bar{z}, \bar{r}, t) = \bar{z}f(\bar{r}, t)$. This linear form is a familiar product of a classic similarity transformation.

C. Mass Balance at the Propellant Surface

In problems for which fluid injection and wall motion are controlled by separate processes, V_b and $\dot{a}$ are independent parameters. In solid propellant rocket motors, however, the relative velocity of the gas with respect to the regressing walls is intimately related to the wall regression speed. To see this, one must recognize that, in any given time interval, the mass of propellant burned must equal the mass of gases ejected into the chamber. Because A_b is the burning surface in a solid propellant motor (or the sublimating surface in a cold-flow simulation of the burning process[47,62,63]) conservation of mass at the solid–gas interface requires that $\rho A_b V_b = \rho_s A_b\dot{a}$. The gas velocity with respect to the wall becomes

$$V_b = (\rho_s/\rho)\dot{a} \tag{8}$$

where ρ_s is the density of the solid phase (before solid propellant pyrolysis or cold-wall sublimation). From Eq. (8), the absolute velocity can be seen to be

$$V = (\rho_s/\rho - 1)\dot{a} = A\dot{a} \tag{9}$$

where $A = \rho_s/\rho - 1$ is the wall permeance or injection coefficient.[59] Because $A \equiv V/\dot{a}$, it is a measure of wall permeability. In rocket motors, $\rho_s \sim 2000\ \mathrm{kgm}^{-3}$, $\rho \sim 20\ \mathrm{kg}\cdot\mathrm{m}^{-3}$, so that $A \sim 100$.

D. Similarity in Space

The condition of incompressibility enables us to use the Stokes stream function $\bar{\psi}$ and reduce the Navier–Stokes equations. Starting with

$$\bar{u}_z = \frac{1}{\bar{r}}\frac{\partial\bar{\psi}}{\partial\bar{r}}, \qquad \bar{u}_r = -\frac{1}{\bar{r}}\frac{\partial\bar{\psi}}{\partial\bar{z}} \tag{10}$$

one may follow Goto and Uchida[59] and write the stream function in a form that is consistent with mass conservation, namely, a Proudman–Johnson form[60] that can lead to a linear $\bar{z}$ variation in the axial velocity. Thus, let we

$$\bar{\psi} = \nu\bar{z}\bar{F}(r, t), \qquad r = \bar{r}/a(t) \tag{11}$$

In terms of $\bar{F}$, the axial and radial velocities become

$$\bar{u}_z = \frac{1}{\bar{r}}\frac{\partial \bar{\psi}}{\partial \bar{r}} = \frac{1}{\bar{r}}\frac{\partial(\nu \bar{z}\bar{F})}{\partial \bar{r}} = \frac{\nu \bar{z}}{a^2}\frac{1}{r}\frac{\partial \bar{F}}{\partial r} \tag{12}$$

$$\bar{u}_r = -\frac{1}{\bar{r}}\frac{\partial \bar{\psi}}{\partial \bar{z}} = -\frac{1}{\bar{r}}\frac{\partial(\nu \bar{z}\bar{F})}{\partial \bar{z}} = -\frac{\nu}{a}\frac{\bar{F}}{r} \tag{13}$$

Because the radial velocity is independent of $\bar{z}$, vorticity simplifies into $\bar{\Omega} = |\nabla \times \bar{\boldsymbol{u}}| = -\partial \bar{u}_z/\partial \bar{r}$. The vorticity transport equation becomes $\bar{\Omega}_t + \bar{\boldsymbol{u}} \cdot \nabla \bar{\Omega} = \nu \nabla^2 \bar{\Omega}$, namely,

$$\frac{\partial}{\partial \bar{r}}\left(\frac{\partial \bar{u}_z}{\partial t}\right) + \frac{\partial}{\partial \bar{r}}\left(\bar{u}_z \frac{\partial \bar{u}_z}{\partial \bar{z}}\right) + \frac{\partial}{\partial \bar{r}}\left(\bar{u}_r \frac{\partial \bar{u}_z}{\partial \bar{r}}\right) - \nu \frac{\partial}{\partial \bar{r}}\left[\frac{1}{\bar{r}}\frac{\partial}{\partial \bar{r}}\left(\bar{r}\frac{\partial \bar{u}_z}{\partial \bar{r}}\right)\right] = 0 \tag{14}$$

To apply Eqs. (11–13), partial derivatives must be carefully evaluated. These involve

$$\frac{\partial \bar{u}_z}{\partial t} = \frac{\nu \bar{z}}{a^2}\frac{\partial}{\partial t}\left(\frac{\bar{F}_r}{r}\right) - \frac{2\nu \bar{z}}{a^3}\frac{\bar{F}_r}{r}\dot{a}$$

$$\frac{\partial \bar{u}_z}{\partial \bar{r}} = \frac{\nu \bar{z}}{a^3}\frac{\partial}{\partial r}\left(\frac{\bar{F}_r}{r}\right), \qquad \frac{\partial \bar{u}_z}{\partial \bar{z}} = \frac{\nu}{a^2}\frac{\bar{F}_r}{r} \tag{15}$$

$$\bar{u}_r \frac{\partial \bar{u}_z}{\partial \bar{r}} = -\frac{\nu^2 \bar{z}}{a^4}\frac{\bar{F}}{r}\frac{\partial}{\partial r}\left(\frac{\bar{F}_r}{r}\right), \qquad \bar{u}_z \frac{\partial \bar{u}_z}{\partial \bar{z}} = \frac{\nu^2 \bar{z}}{a^4}\left(\frac{\bar{F}_r}{r}\right)^2$$

$$\frac{1}{\bar{r}}\frac{\partial}{\partial \bar{r}}\left(\bar{r}\frac{\partial \bar{u}_z}{\partial \bar{r}}\right) = \frac{\nu \bar{z}}{a^4}\frac{1}{r}\frac{\partial}{\partial r}\left[r\frac{\partial}{\partial r}\left(\frac{\bar{F}_r}{r}\right)\right] \tag{16}$$

E. Reduced Navier–Stokes Equation

Substituting Eqs. (15) and (16) into Eq. (14) yields

$$\Big\{(-\nu \bar{z}/a^3)(\bar{F}_{rt}/r) + (\dot{a}\nu \bar{z} r/a^4)(\bar{F}_r/r)_r + (2\nu \dot{a}/a^4)(\bar{z}/r)\bar{F}_r - (\nu^2 \bar{z}/a^5)(\bar{F}_r/r)^2 + (\nu^2 \bar{z}/a^5)(\bar{F}/r)(\bar{F}_r/r)_r + (1/r)(\bar{F}_r/r)_r + (\bar{F}_r/r)_{rr}\Big\}_r = 0 \tag{17}$$

At this point, it is expedient to introduce the dimensionless regression ratio

$$\alpha(t) \equiv \dot{a}a/\nu \tag{18}$$

where α is a Reynolds number based on the regression speed of the walls. Inserting Eq. (18) into Eq. (17) renders, after some algebra, the Proudman–Johnson-type equation[60]

$$\Big\{(\bar{F}_r/r)_{rr} + [(1+\bar{F})/r + \alpha r](\bar{F}_r/r)_r - (\bar{F}_r/r - 2\alpha)\bar{F}/r - (a^2/\nu)(\bar{F}_{rt}/r)\Big\}_r = 0 \tag{19}$$

Boundary conditions may be obtained from Eq. (4). These translate into

$$\bar{F}_r/r = 0, \qquad \bar{F}/r = Re \qquad \text{at} \qquad r = 1 \tag{20}$$

$$(\bar{F}_r/r)_r = 0, \qquad \bar{F}/r = 0 \qquad \text{at} \qquad r = 0 \tag{21}$$

where $Re \equiv Va/\nu$ is the dynamic Reynolds number based on the absolute injection velocity. Equation (19) embraces Yuan and Finkelstein's[61] and is consistent with that solved numerically by Goto and Uchida.[59] Note that Re and α are generally unrelated. However, for cases involving propellant combustion or solid-phase sublimation, Eq. (9) can be multiplied by a/ν to obtain $Re = A\alpha$. Under these auspices, Re and α become intimately related by the solid-to-gas density ratio. For illustrative purposes, a range of physical parameters corresponding to solid propellants is taken from Sutton[64] and compiled in Table 1 (cf., Ref. 64, pp. 370, 375, 418, and 435). We note that data regarding viscosity are based on the model by Lucas, which remains applicable at high temperatures and pressures (see Ref. 65). We also note that the maximum regression speed is taken from a recent work by Beckstead.[66]

Table 1 Range of parameters for solid rocket motors

Parameter	Symbol	Range
Grain radius, m	a	0.005–3.5
Grain density, kgm^{-3}	ρ_s	1,500–2,500
Gas density, kgm^{-3}	ρ	10–20
Kinematic viscosity, m^{2}s^{-1}	ν	10^{-6}–10^{-5}
Grain burn rate, ms^{-1}	$\dot{a}$	0.0005–0.1
Gas injection velocity, ms^{-1}	V_b	0.0075–10
Regression ratio	α	0.125–35,000
Injection Reynolds number	Re	35–3.3×10^6

F. Similarity in Time

To make further headway toward a more manageable equation, we assume a self-similarity in time that can be reasonably justified in practice. Using the same argument presented by Uchida and Aoki,[67] we first apply the transformation $\bar{F}(r,t) \to \bar{F}[r, \alpha(t)]$ and then define α to be invariant in time. To realize this condition, α must be specified by its initial value, namely,

$$\alpha = \dot{a}a/\nu = \dot{a}_0 a_0/\nu \tag{22}$$

where a_0 and $\dot{a}_0$ represent the initial radius and regression rate. The ensuing transformation can be arrived at by integrating Eq. (22) with respect to time. One obtains

$$a(t) = a_0\sqrt{1 + 2\nu\alpha t a_0^{-2}} \tag{23}$$

From a physical standpoint, our idealization is based on a decelerating regression rate that follows a plausible model according to which $a\dot{a} = \text{const}$. Thus, as the internal radius increases, the rate of regression decreases. Far from being general, this limiting feature is used to permit a closed-form solution. In actual rocket motors, one must recognize that propellant burning exhibits a more complex regression behavior.

G. Idealized Thrust Behavior

Pursuant to the mass conservation details in Sec. II.B, one may apply the integral form of momentum conservation to estimate the axial thrust force due to gas ejection. Using β to represent the $\mathcal{O}(1)$ momentum correction coefficient, one gets

$$F = \int_{A_c} \rho \bar{u}^2(\bar{z}, \bar{r}, t)\, \mathrm{d}A = \beta \rho A_c \bar{u}_m^2$$

$$\beta \equiv A_c^{-1}\bar{u}_m^{-2}\int_{A_c} \bar{u}^2(\bar{z}, \bar{r}, t)\, \mathrm{d}A \tag{24}$$

Then, from Eq. (7), one can substitute the value for the mean axial velocity $\bar{u}_m$ and cross-sectional area A_c to obtain

$$F = \beta\rho\pi a^2[2L(V_b - \dot{a})/a]^2 = 4\pi\beta\rho L^2(V_b - \dot{a})^2 \tag{25}$$

Imposition of $a\dot{a} = \alpha\nu = \text{const}$ gives

$$F = 4\pi\beta\rho L^2[V_b - \alpha\nu/a(t)]^2 \tag{26}$$

Thus, in cold-flow experiments having fixed blowing speed with respect to the wall ($V_b = \text{const}$), the thrust force will increase according to Eq. (26) as the internal radius of the chamber increases in time.

In a solid propellant rocket motor, however, the injection speed with respect to the moving wall is related to both the propellant density along the burning interface and the speed of regression via Eq. (8). At the outset, Eq. (25) becomes

$$F = 4\pi\beta\rho L^2(\rho_s/\rho - 1)^2\dot{a}^2 = 4\pi\beta\rho L^2(\alpha\nu)^2 A^2/a^2 \sim A^2/a^2 \tag{27}$$

Because $A = \rho_s/\rho - 1$ is constant for a homogeneous propellant (where the solid propellant density ρ_s remains uniform), Eq. (27) suggests a regressive thrust with increasing $a(t)$. Nonetheless, a neutral thrust is also conceivable by designing a propellant whose density ratio increases proportionately with the inner radius according to $A \sim a(t)$. Similarly, a progressive thrust can be accomplished by designing a propellant with a density ratio that increases at a faster rate than the radius, that is, for A/a increasing in time.

H. Self-Similarity Solution in Time and Space

Under the provision of a time invariant α, we find it useful to define

$$F \equiv \bar{F}/Re, \qquad \eta \equiv \tfrac{1}{2}r^2, \qquad \varepsilon \equiv 1/Re \tag{28}$$

Backward substitution into Eq. (19) yields

$$\varepsilon\left[2\eta\frac{\mathrm{d}^4F}{\mathrm{d}\eta^4} + (2\alpha\eta + 3)\frac{\mathrm{d}^3F}{\mathrm{d}\eta^3} + 4\alpha\frac{\mathrm{d}^2F}{\mathrm{d}\eta^2}\right] + F\frac{\mathrm{d}^3F}{\mathrm{d}\eta^3} - \frac{\mathrm{d}F}{\mathrm{d}\eta}\frac{\mathrm{d}^2F}{\mathrm{d}\eta^2} = 0 \tag{29}$$

with

$$\frac{\mathrm{d}F\left(\frac{1}{2}\right)}{\mathrm{d}\eta} = 0, \qquad F\left(\tfrac{1}{2}\right) = 1, \qquad F(0) = 0$$

$$\lim_{\eta \to 0}\sqrt{2\eta}\frac{\mathrm{d}^2F}{\mathrm{d}\eta^2} = 0 \tag{30}$$

Next, we solve this set using asymptotic tools.

III. Analytical Solution

Following Terrill and Thomas[21] and Terrill,[68] we start by expanding $F = F_0 + \varepsilon F_1 + \mathcal{O}(\varepsilon^2)$ and substitute back into Eq. (29). At leading order, a basic solution is obtained, namely,

$$F_0\frac{\mathrm{d}^3F_0}{\mathrm{d}\eta^3} - \frac{\mathrm{d}F_0}{\mathrm{d}\eta}\frac{\mathrm{d}^2F_0}{\mathrm{d}\eta^2} = 0 \tag{31}$$

The solution to this equation can be guessed to be $F_0 = \sin(\pi\eta)$. When $\theta \equiv \pi\eta$ is defined, the first-order equation of $\mathcal{O}(\varepsilon)$ may now be written as

$$\sin\theta\frac{\mathrm{d}^3F_1}{\mathrm{d}\theta^3} - \cos\theta\frac{\mathrm{d}^2F_1}{\mathrm{d}\theta^2} + \sin\theta\frac{\mathrm{d}F_1}{\mathrm{d}\theta} - \cos\theta F_1 = \left(\frac{2}{\pi}\alpha\theta + 3\right)\cos\theta + \frac{4}{\pi}\alpha\sin\theta - 2\theta\sin\theta \tag{32}$$

A. Variation of Parameters

To make headway, one must guess that a partial solution must be $F_{1h} = \cos\theta$. The variation of parameters approach can then be used to find the correction multiplier based on $F_{1h} = C(\theta)\cos\theta$. Thus, backward substitution into the homogeneous part of Eq. (32) yields

$$C'''\sin\theta\cos\theta - 2C''\sin^2\theta - C'' = 0 \tag{33}$$

so that

$$C(\theta) = K_0\tan\theta + K_1\theta + K_2 \tag{34}$$

The complete homogeneous solution becomes

$$F_{1h} = K_0\sin\theta + K_1\theta\cos\theta + K_2\cos\theta \tag{35}$$

where K_0, K_1, and K_2 are yet to be determined. The method of variation of parameters is applied once more by turning the three integration constants into undetermined functions. Thus, we set

$$F_1(\theta) = K_0(\theta)\sin\theta + K_1(\theta)\theta\cos\theta + K_2(\theta)\cos\theta \tag{36}$$

Substituting Eq. (36) into Eq. (32) leads to

$$K_0'\sin\theta + K_1'\theta\cos\theta + K_2'\cos\theta = 0 \tag{37}$$

$$K_0'\cos\theta + K_1'(\cos\theta - \theta\sin\theta) - K_2'\sin\theta = 0 \tag{38}$$

$$K_0'\sin^2\theta + K_1'(2\sin^2\theta + \theta\cos\theta\sin\theta) + K_2'\cos\theta\sin\theta = -[(2\alpha/\pi)\theta + 3]\cos\theta + (4\alpha/\pi)\sin\theta - 2\theta\sin\theta \tag{39}$$

Solving Eqs. (37–39) simultaneously enables us to determine the variable coefficients. These are found to be

$$K_0 = (\alpha/\pi)\left[-\theta\csc\theta + 3\ln\tan\tfrac{1}{2}\theta + (\cos\theta - \theta\sin\theta)\right] - \tfrac{3}{2}\csc\theta - \tfrac{1}{2}\sin\theta - \theta\cos\theta - S(\theta) + C_0 \tag{40}$$

$$K_1 = (\alpha/\pi)\left(\theta\csc\theta - 3\ln\tan\tfrac{1}{2}\theta\right) + \tfrac{3}{2}\csc\theta + S(\theta) + C_1 \tag{41}$$

$$K_2 = (\alpha/\pi)[3S(\theta) - \theta\cos\theta - \sin\theta - \theta^2\csc\theta] - \tfrac{1}{2}\cos\theta + \theta\sin\theta - \tfrac{3}{2}\theta\csc\theta - S_1(\theta) + C_2 \tag{42}$$

where

$$S(\theta) = \int_0^\theta \phi\csc\phi\,\mathrm{d}\phi, \qquad S_1(\theta) = \int_0^\theta \phi^2\csc\phi\,\mathrm{d}\phi \tag{43}$$

In series form, these integrals become

$$S(x) = x + \sum_{k=1}^{\infty}\frac{2}{\pi^{2k}}\left(\sum_{n=1}^{\infty}\frac{1}{n^{2k}}\right)\frac{(1-2^{1-2k})}{(2k+1)}x^{2k+1}$$

$$S_1(x) = \frac{1}{2}x^2 + \sum_{k=1}^{\infty}\left(\sum_{n=1}^{\infty}n^{-2k}\right)\frac{(1-2^{1-2k})}{(k+1)\pi^{2k}}x^{2k+2} \tag{44}$$

B. First-Order Solution

To recapitulate, we recall that $\theta = \pi\eta$ and combine the basic and first-order solutions for F. We obtain

$$F = \sin\theta + \varepsilon\left\{(\alpha/\pi)\left[3\ln\tan\tfrac{1}{2}\theta(\sin\theta - \theta\cos\theta) - 2\theta\right] - 2 + (\theta\cos\theta - \sin\theta)S(\theta) + [3(\alpha/\pi)S(\theta) - S_1(\theta)]\cos\theta + C_0\theta\cos\theta + C_1\sin\theta + C_2\cos\theta\right\} \tag{45}$$

The remaining constants can be determined from the boundary conditions given by Eq. (30). One finds

$$C_0 = -(4/\pi) + (2\alpha/\pi^2 - 1) - S\left(\tfrac{1}{2}\pi\right)(6\alpha/\pi^2 + 1) + (2/\pi)S_1\left(\tfrac{1}{2}\pi\right) \tag{46}$$

$$C_1 = \left[\alpha + 2 + S\left(\tfrac{1}{2}\pi\right)\right], \qquad C_2 = 2 \tag{47}$$

At this juncture, the axial and radial components of velocity and pressure can be evaluated. One finds Culick's[19] or Yuan and Finkelstein's[61] components to be recoverable from Eqs. (45–47). Because it is asymptotic in nature, Eq. (45) can faithfully reproduce viscous and regression effects so long as ε and $\varepsilon\alpha$ are small, respectively. Practically, the range of applicability encompasses both cold-flow and rocket motor applications wherein both ε and $\varepsilon\alpha$ are smaller than 0.1.

To avoid singularities at the core, however, we resort to η as our independent coordinate for calculations and plots. To maintain generality, we present variables in the following dimensionless form:

$$z = \bar{z}/a, \qquad \psi = \bar{\psi}/a^2V = zF$$

$$\Omega = \bar{\Omega}a/V = -z(F_r/r)_r = -z\sqrt{2\eta}F_{\eta\eta}, \qquad p = \bar{p}/\rho V^2 \tag{48}$$

$$u_r = \bar{u}_r/V = -F/r = -F\Big/\sqrt{2\eta}$$

$$u_z = \bar{u}_z/V = (z/r)F_r = zF_\eta, \qquad u_m = \bar{u}_m/V = 2z \tag{49}$$

Pursuant to these choices, the axial velocity normalized by the mean axial velocity becomes $u_z/u_m = \frac{1}{2}F_\eta$. In like fashion, the normalized radial pressure loss measured from the core can be determined. Starting with

$$p_\eta = -\left[\varepsilon F_\eta + \alpha\varepsilon F + (F/\eta)^2\right]_\eta \tag{50}$$

one may integrate from the core to any radial position. The resulting drop is found to be

$$\Delta p_r \equiv -[p(\eta, z) - p(0, z)] = \varepsilon F_\eta + \alpha\varepsilon F + \eta^{-1}\left(\tfrac{1}{2}F\right)^2 - \varepsilon F_\eta(0) \tag{51}$$

Similarly, the axial pressure drop measured from the head end can be written as

$$\Delta p_z \equiv p(\eta, z) - p(\eta, 0) = \tfrac{1}{2}z^2\left\{\varepsilon\left[\left(\alpha + \tfrac{1}{2}\eta^{-1}\right)F_\eta + 2\eta F_{\eta\eta\eta} + (2\alpha\eta - 1)F_{\eta\eta}\right] - (F_\eta)^2 + FF_\eta(1 - \eta^{-1})\right\} \quad (52)$$

Finally, the shear stress may be determined from Newton's law for viscosity. One finds

$$\tau = \bar{\tau}/\rho V^2 = -\mu\bar{\Omega}/\rho V^2 = \varepsilon z\sqrt{2\eta}F_{\eta\eta} = -\varepsilon\Omega \quad (53)$$

where the linear relation with mean-flow vorticity is apparent. At the wall, Eq. (53) gives $\tau_b = \varepsilon z F_{\eta\eta}(\frac{1}{2}) = -\varepsilon\Omega(1)$.

IV. Illustrations

To examine the effects of viscosity and wall regression, the main flow attributes are now described over different ranges of the control variables. This description is hoped to aid in interpreting the significance and limitations of the higher-order approximation. This is accomplished by observing the behavior of flow streamlines, velocities, pressure distributions, and shearing stresses at the wall.

A. Streamlines

In Fig. 2, streamline patterns are shown for two disparate values of the Reynolds number, both with and without wall regression. From Fig. 2a, it may be inferred that, in the absence of wall motion, only slight differences in streamline curvatures arise near the head end despite the two orders of magnitude separating the Reynolds numbers. Differences in streamline curvatures and, hence, the flow turning speed, become more appreciable in the downstream portions. One expects these differences to be more pronounced in elongated rocket motors. The effects of viscosity are clearly more significant in the downstream sections of the tube. Thus, as the Reynolds number is decreased from 1000 to 10, the viscous decay of the radial velocity component takes place more rapidly. As a result, the flow turning speed is increased, leading to a sharper streamline curvature near the walls.

Figure 2b, on the other hand, indicates that lowering the Reynolds number causes the flow to become more sensitive to changes in wall regression. This explains the incapacity of (large Reynolds number *Re*) inviscid flows in capturing the wall motion. As can be inferred by inspection of Eq. (29), the determining factor appears to be α/Re or $1/A$. The smaller this factor is, the less sensitive the flow will be and the more closely will it resemble the inviscid analog. Far downstream, however, the otherwise negligible discrepancies between viscous and inviscid flows with either stationary or expanding walls are magnified. This is due to the downstream propagation and buildup in cumulative errors caused by suppressing viscous diffusion. As confirmed by Lee and Beddini,[29,30] retention of viscous effects is clearly necessary, especially when tracking the inception of turbulence in the presence of periodic disturbances. Figure 2b also indicates that the effect of fast wall expansion is to reduce the flow turning speed, for example, for $Re = 10$. The higher the regression speed, the longer will the radial-to-axial velocity ratio be large while approaching the core. The curvature of an incoming streamline is, thus, increased with $\dot{a}$. A purely hypothetical case arises, for instance, when the walls regress at nearly the same speed as that of the fluid entering the tube, that is, $\dot{a} = V_b$. Under such conditions, the expansion process offsets the effect of injection to the point of forcing streamlines to become perpendicular to the walls.

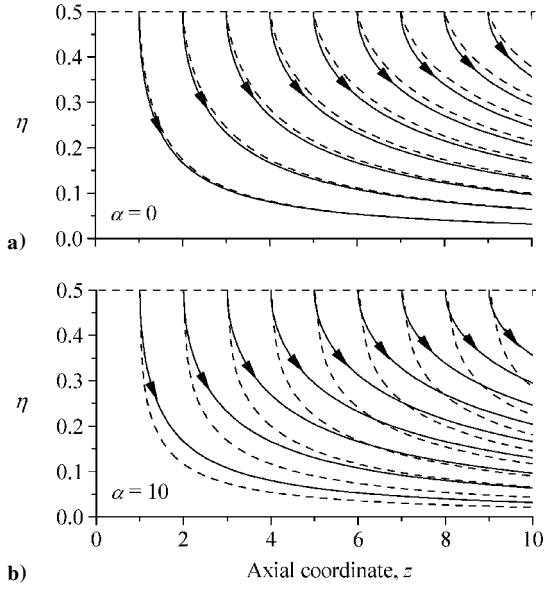

Fig. 2 Influence of the regression rate on the streamlines for – – –, *Re* = 10 and ——, *Re* = 1000.

B. Axial Velocity

Figures 3 and 4 show the behavior of axial velocity profiles (normalized by their mean values u_m) over a range of Reynolds number *Re* and α. Similar trends to those associated with streamline curvatures may be observed. Specifically, a greater sensitivity to

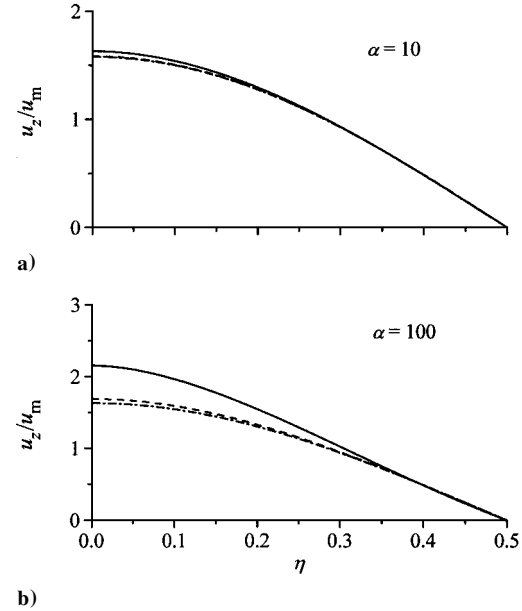

Fig. 3 Influence of the regression rate on the axial velocity for ——, *Re* = 100; – – –, *Re* = 500; and –·–, *Re* = 1000.

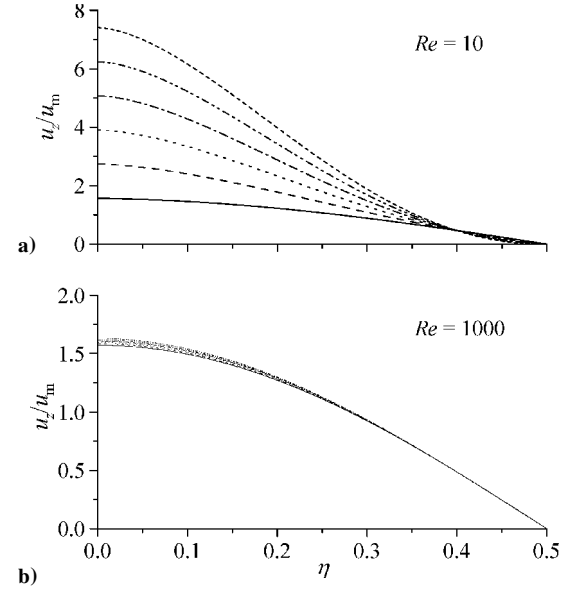

Fig. 4 Sensitivity of the axial velocity to the regression rate (——, 0; – – –, 20; - - - -, 40; –·–, 60; –···–, 80; and · · · ·, 100): at a) moderate injection Reynolds number and b) large injection Reynolds number.

wall regression is observed at smaller values of Reynolds number Re. Figure 3 indicates that, as α changes from 10 (Fig. 3a) to 100 (Fig. 3b), the centerline velocity increases from 1.63 to 2.15 times the average velocity for a Reynolds number of 100. This 32% increase in the centerline-to-mean velocity ratio is quite significant by comparison to the 7 and 3% increases observed at $Re = 500$ and 1000, respectively. The reduced sensitivity to wall motion can be attributed to the diminished role of viscosity at a higher Reynolds number. Note that, when the walls are made permeable and allowed to expand, the 2.15 overshoot over u_m (shown in Fig. 3b) exceeds the factor of 2 associated with a fully developed Poiseuille flow in a tube. The increased centerline-to-mean velocity ratio in a porous-walled channel can be ascribed to the injection stream, whose contribution to the axial velocity is a skewed spatial function that is largest along the centerline.

For fixed Reynolds number Re, the regression rate is now varied by equal increments in Fig. 4 over the range 0–100. In Fig. 4a, a significant variation in the centerline-to-mean velocity ratio is observed ranging from 1.57 to 7.41 as α is increased from 0 to 100. This 372% speed augmentation at the centerline can be achieved or even exceeded when α is prescribed in a manner to be of the same order or larger than Re. When this is no longer the case, such as in Fig. 4b (where $Re = 1000$), the mean-flow overshoot at the centerline is increased only from 1.57 to 1.63; this marks a mere 4% magnification for the same variation in α. We conclude that the centerline-to-mean velocity overshoot is sensitive to the relative expansion speed and, therefore, commensurate with the size of α/Re. For sufficiently small α/Re, the centerline-to-mean velocity ratio asymptotes to 1.57 or $\frac{1}{2}\pi$. This ratio is due to the mean velocity being $2z$ according to Eq. (49) and to the inviscid axial velocity being $u_z(r, z) = \pi z \cos(\frac{1}{2}\pi r^2)$ and hence equal to πz at the centerline. It also coincides with the center-to-mean velocity ratio in a planar channel. In the latter case, $u_z(x, y) = \frac{1}{2}\pi x \cos(\frac{1}{2}\pi y)$ or $\frac{1}{2}\pi x$ along the midsection plane, whereas the mean velocity is simply x (Ref. 53).

From a practical perspective, Fig. 4 clearly indicates that the effect of regression can be considerable in comparison to the solution with stationary walls. Because most current mathematical and numerical models ignore regression effects, this study demonstrates that there are certain ranges over which one must not discount regression without incurring significant errors. The amount of error depends, of course, on the relative orders of α and Reynolds number Re. As indicated earlier, in a recent simulation of a slab rocket motor in two-space dimensions, Venugopal et al.[56] have employed an injection Reynolds number of 47.6 throughout their investigation. Nonetheless, no regression was incorporated in their numerical model. The results of this study suggest that for a typical regression rate of 100, the influence of wall regression can be so important at such a value of Reynolds number Re ($\approx$48) that its incorporation appears to be a necessity.

C. Radial Velocity

The radial velocity is shown in Fig. 5 for three different values of the relative regression rate α/Re. At the outset, two interesting phenomena are observed. The first corresponds to the existence of a point along the interval $0 < \eta < \frac{1}{2}$, where the radial velocity exceeds its (absolute) value at the wall. At first glance, this behavior appears paradoxical because u_r is expected to diminish monotonically while approaching the centerline. At least, this was the trend observed in the slab rocket motor analog.[53] The difference here lies in the existence of a finite curvature to which one can attribute the near-wall overshoot. The reason is this: Because the cylindrical flow area $A_n(r) = 2\pi r L$ normal to incoming streams is proportional to the radius, the sudden reduction in A_n in the vicinity of the wall (where the axial velocity is insignificant) forces the radial velocity to increase (in absolute value) to keep satisfying mass conservation. The second interesting phenomenon is observed when the relative expansion ratio increases. In this event, because expansion delays flow turning, the point of maximum radial velocity moves away from the wall. This is clearly shown in Fig. 5 for $Re = 100$. Past that point of maximum radial velocity, the axial component is no longer insignificant. The downstream mass transport becomes sufficiently appreciable to offset the effect of a radial compression in A_n. For the three cases shown at $\alpha/Re = 1$, 0.2, and 0.1, the radial velocity overshoot relative to the wall is found to be 1.236, 1.087, and 1.076 at $r = 0.707$, 0.828, and 0.845; they indicate that the distance from the wall to the point of maximum u_r is commensurate with the size of α/Re. We conclude that the closest distance to the wall together with the smallest overshoot occur when either 1) the walls are not moving or 2) the Reynolds number is very high. From the inviscid formulation, one finds that the smallest possible overshoot is 1.07 at a radius of 0.861.

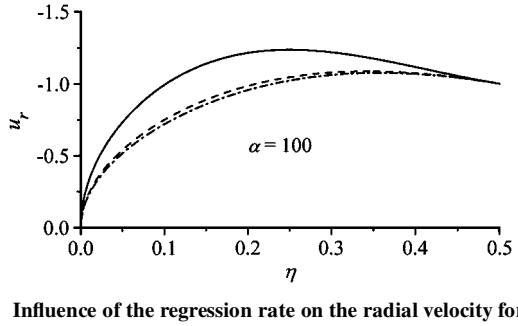

Fig. 5 Influence of the regression rate on the radial velocity for ——, Re = 100; – – –, Re = 500; and –·–, Re = 1000.

D. Radial and Axial Pressure Distribution

The pressure difference given by Eq. (51) is plotted in Fig. 6 for fixed α and a range of Reynolds number Re (Fig. 6a) and fixed Reynolds number Re and a range of α (Fig. 6b). The drop is always positive, indicating, a higher pressure along the centerline. Consistent with the radial velocity distribution, the pressure drop exhibits a maximum on the interval $0 < \eta < \frac{1}{2}$. As shown in Fig. 6a, for $\alpha/Re = 1$, 0.2, and 0.1, extrema of 1.66, 0.77, and 0.67 appear at $r = 0.783$, 0.854, and 0.859. These locations are 11, 3, and 1.7% closer to the wall than the loci of maximum radial velocities. Both the wall distance and magnitude of the overshoot seem to decrease with successive decreases in α/Re. These trends are further confirmed in Fig. 6b where, due to comparable sizes of α and Re, significant overshoot values in the pressure drop are realized at increasing distances from the wall. Consistent with Eq. (52), the axial pressure diminishes in a parabolic fashion along the axis of the tube. Its dependence on α/Re follows the same physical arguments presented earlier.

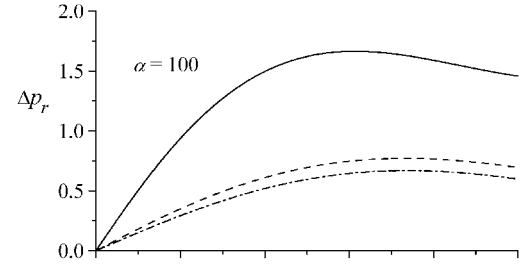

Fig. 6a Influence of the injection Reynolds number on the radial pressure distribution for ——, Re = 100; – – –, Re = 500; and –·–, Re = 1000.

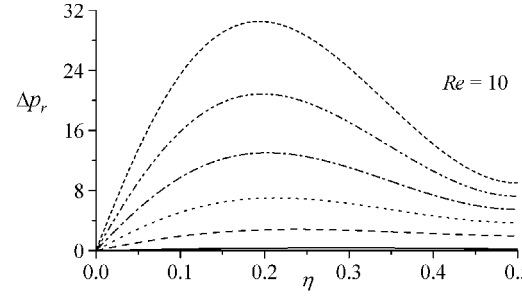

Fig. 6b Radial pressure distribution at a moderate injection Reynolds number and a range of regression rates: ——, 0; – – –, 20; - - - -, 40; –·–, 60; -···-, 80; and · · · ·, 100.

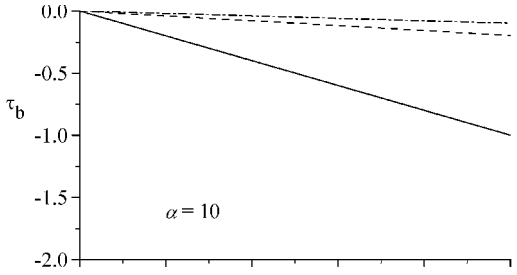

Fig. 7a Influence of the injection Reynolds number on the wall shear stress for a moderate regression rate and ——, *Re* = 100; – – –, *Re* = 500; and –·–, *Re* = 1000.

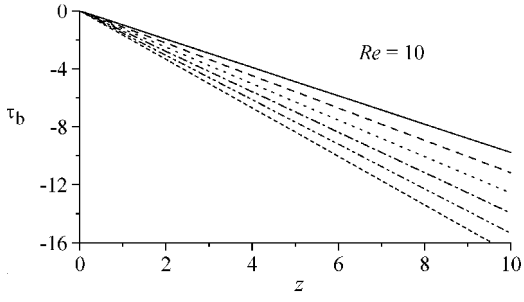

Fig. 7b Wall shear stress at a moderate injection Reynolds number and a range of regression rates: ——, 0; – – –, 20; - - - -, 40; –·–, 60; –···, 80; and · · · ·, 100.

E. Wall Shear Stress

Figure 7 shows the influence of Reynolds number *Re* and α on the shear stress (or vorticity) along the regressing surface. For fixed α and a range of Reynolds number *Re*, Fig. 7a confirms that the shear stress at the wall decreases with successive increases in the Reynolds number. This is also true of mean-flow vorticity. Thus, as the role of viscosity is diminished, the friction force is weakened as well.

When the Reynolds number is fixed at $Re = 10$ (Fig. 7b), varying the regression rate of comparable size leads to more appreciable stresses at higher expansion rates. The expansion process may, therefore, be viewed as a mechanism that promotes higher friction at the wall. This stress increases downstream due to the relative growth in the parallel-to-normal velocity ratio. The increased friction also signals larger vorticity production in the downstream portions of the tube.

V. Conclusions

A higher-order mean-flow approximation is presented for an idealized rocket motor. Besides its ability to account for wall regression, the final solution is consistently viscous and rotational. As such, it is suitable for use in the fundamental aeroacoustic solution that has received much scrutiny in the past. It can also be used to investigate, by way of linear stability theory, the hydrodynamic evolution of the core-flow shear layers. In past studies, the onset of instability has invariably evolved from the introduction of periodic fluctuations bearing the form $F \exp[i(kz - \omega t)]$; therein, $F = \sin(\frac{1}{2}\pi r^2)$ and (k, ω) have been used to symbolize the complex wave number and frequency of oscillations, respectively.[26] Instead of analyzing the transition to turbulence based on an inviscid function, it is now possible to incorporate the viscous correction given by Eq. (45) into the expression for F. It may be safely argued that a more accurate assessment of the hydrodynamic transition maps can be developed therefrom. A more precise characterization of the acoustic boundary layer can also be expected including mean-flow adjustments in the critical parameters leading to turbulence.[29,30] Overall, the demonstrated applicability of the current approximation to a broader range of physical parameters extends its usage to problems for which the inviscid solution deteriorates. These include high-acceleration interceptor vehicles that utilize fast regressing propellants. They also encompass cold-flow experiments that involve medium-to-large injection. In the future, it is hoped that the mathematical details provided here can be used to overcome the nonlinear behavior arising in similar equations of higher order.

Acknowledgments

The authors wish to thank the anonymous reviewers for their helpful recommendations. We are especially grateful for the suggestion that has led to Sec. II.G in which the idealized thrust character is examined in light of the analytical approximation.

References

[1]Taylor, G. I., "Fluid Flow in Regions Bounded by Porous Surfaces," *Proceedings of the Royal Society, London, Series A: Mathematical and Physical Sciences*, Vol. 234, No. 1199, 1956, pp. 456–475.

[2]Peng, Y., and Yuan, S. W., "Laminar Pipe Flow with Mass Transfer Cooling," *Journal of Heat Transfer*, Vol. 87, No. 2, 1965, pp. 252–258.

[3]Yuan, S. W., "Cooling by Protective Fluid Films," *Turbulent Flows and Heat Transfer*, edited by C. C. Lin, Sec. G, Vol. 5, Princeton Univ. Press, Princeton, NJ, 1959, pp. 428–488.

[4]Berman, A. S., "Laminar Flow in Channels with Porous Walls," *Journal of Applied Physics*, Vol. 24, No. 9, 1953, pp. 1232–1235.

[5]Berman, A. S., "Effects of Porous Boundaries on the Flow of Fluids in Systems with Various Geometries," *Proceedings of the Second United Nations International Conference on the Peaceful Uses of Atomic Energy*, Ser. P/720, Vol. 4, United Nations, Geneva, 1958, pp. 351–358.

[6]Berman, A. S., "Laminar Flow in an Annulus with Porous Walls," *Journal of Applied Physics*, Vol. 29, No. 1, 1958, pp. 71–75.

[7]Acrivos, A., "The Asymptotic Form of the Laminar Boundary-Layer Mass-Transfer Rate for Large Interfacial Velocities," *Journal of Fluid Mechanics*, Vol. 12, No. 3, 1962, pp. 337–357.

[8]Leadon, B. M., "The Status of Heat Transfer Control by Mass Transfer for Permanent Surface Structures," *Aerodynamically Heated Structures*, edited by P. E. Glaser, Prentice–Hall, Englewood Cliffs, NJ, 1962, pp. 171–196.

[9]Libby, P. A., "The Homogeneous Boundary Layer at an Axisymmetric Stagnation Point with Large Rates of Injection," *Journal of the Aerospace Sciences*, Vol. 29, No. 1, 1962, pp. 48–60.

[10]Banks, W. H. H., and Zaturska, M. B., "On Flow Through a Porous Annular Pipe," *Physics of Fluids*, Ser. A, Vol. 4, No. 6, 1992, pp. 1131–1141.

[11]Zaturska, M. B., and Banks, W. H. H., "Suction-Driven Flow in a Porous Pipe," *ZAMM*, Vol. 75, No. 1, 1995, pp. 21–30.

[12]Cox, S. M., and King, A. C., "On the Asymptotic Solution of a High-Order Nonlinear Ordinary Differential Equation," *Proceedings of the Royal Society, London, Series A: Mathematical and Physical Sciences*, Vol. 453, No. 1959, 1997, pp. 711–728.

[13]King, J. R., and Cox, S. M., "Asymptotic Analysis of the Steady-State and Time-Dependent Berman Problem," *Journal of Engineering Mathematics*, Vol. 39, March 2001, pp. 87–130.

[14]Lu, C., "On the Asymptotic Solution of Laminar Channel Flow with Large Suction," *SIAM Journal on Mathematical Analysis*, Vol. 28, No. 5, 1997, pp. 1113–1134.

[15]Lu, C., "On the Existence of Multiple Solutions of a Boundary Value Problem Arising from Laminar Flow Through a Porous Pipe," *Canadian Applied Mathematics Quarterly*, Vol. 2, No. 3, 1994, pp. 361–393.

[16]Flandro, G. A., "Effects of Vorticity on Rocket Combustion Stability," *Journal of Propulsion and Power*, Vol. 11, No. 4, 1995, pp. 607–625.

[17]Flandro, G. A., "On Flow Turning," AIAA Paper 95-2530, July 1995.

[18]Flandro, G. A., and Majdalani, J., "Aeroacoustic Instability in Rockets," AIAA Paper 2001-3868, July 2001.

[19]Culick, F. E. C., "Rotational Axisymmetric Mean Flow and Damping of Acoustic Waves in a Solid Propellant Rocket," *AIAA Journal*, Vol. 4, No. 8, 1966, pp. 1462–1464.

[20]Hart, R. W., and McClure, F. T., "Combustion Instability: Acoustic Interaction with a Burning Propellant Surface," *Journal of Chemical Physics*, Vol. 10, No. 6, 1959, pp. 1501–1514.

[21]Terrill, R. M., and Thomas, P. W., "On Laminar Flow Through a Uniformly Porous Pipe," *Applied Scientific Research*, Vol. 21, Aug. 1969, pp. 37–67.

[22]Dunlap, R., Willoughby, P. G., and Hermsen, R. W., "Flowfield in the Combustion Chamber of a Solid Propellant Rocket Motor," *AIAA Journal*, Vol. 12, No. 10, 1974, pp. 1440–1445.

[23]Yamada, K., Goto, M., and Ishikawa, N., "Simulative Study of the Erosive Burning of Solid Rocket Motors," *AIAA Journal*, Vol. 14, No. 9, 1976, pp. 1170–1176.

[24]Varapaev, V. N., and Yagodkin, V. I., "Flow Stability in a Channel with Porous Walls," *Fluid Dynamics (Izvestiya Akademii Nauk SSSR, Meckanika Zhidkosti i Gaza)*, Vol. 4, No. 5, 1969, pp. 91–95.

[25]Casalis, G., Avalon, G., and Pineau, J.-P., "Spatial Instability of Planar Channel Flow with Fluid Injection Through Porous Walls," *Physics of Fluids*, Vol. 10, No. 10, 1998, pp. 2558–2568.

[26]Griffond, J., Casalis, G., and Pineau, J.-P., "Spatial Instability of Flow in a Semiinfinite Cylinder with Fluid Injection Through Its Porous Walls," *European Journal of Mechanics B/Fluids*, Vol. 19, No. 1, 2000, pp. 69–87.

[27]Hart, R. W., Bird, J. F., Cantrell, R. H., and McClure, F. T., "Nonlinear Effects in Instability of Solid Propellant Rocket Motors," *AIAA Journal*, Vol. 2, No. 7, 1964, pp. 1270–1273.

[28]Hart, R. W., and McClure, F. T., "Theory of Acoustic Instability in Solid Propellant Rocket Combustion," *Tenth Symposium (International) on Combustion*, Combustion Inst., Pittsburgh, PA, 1964, pp. 1047–1066.

[29]Lee, Y., and Beddini, R. A., "Effect of Solid Rocket Chamber Pressure on Acoustically Induced Turbulent Transition," AIAA Paper 2000-3802, 2000.

[30]Lee, Y., and Beddini, R. A., "Acoustically Induced Turbulent Transition in Solid Propellant Rocket Chamber Flowfields," AIAA Paper 99-2508, 1999.

[31]Beddini, R. A., and Roberts, T. A., "Turbularization of an Acoustic Boundary Layer on a Transpiring Surface," *AIAA Journal*, Vol. 26, No. 8, 1988, pp. 917–923.

[32]Sabnis, J. S., Gibeling, H. J., and McDonald, H., "Navier–Stokes Analysis of Solid Propellant Rocket Motor Internal Flows," *Journal of Propulsion and Power*, Vol. 5, No. 6, 1989, pp. 657–664.

[33]Tissier, P. Y., Godfroy, F., and Jacquemin, P., "Simulation of Three Dimensional Flows Inside Solid Propellant Rocket Motors Using a Second-Order Finite Volume Method: Application to the Study of Unstable Phenomena," AIAA Paper 92-3275, July 1992.

[34]Roh, T. S., Tseng, I. S., and Yang, V., "Effects of Acoustic Oscillations on Flame Dynamics of Homogeneous Propellants in Rocket Motors," *Journal of Propulsion and Power*, Vol. 11, No. 4, 1995, pp. 640–650.

[35]Apte, S., and Yang, V., "Effects of Acoustic Oscillations on Turbulent Flowfield in a Porous Chamber with Surface Transpiration," AIAA Paper 98-3219, July 1998.

[36]Avalon, G., Casalis, G., and Griffond, J., "Flow Instabilities and Acoustic Resonance of Channels with Wall Injection," AIAA Paper 98-3218, July 1998.

[37]Lupoglazoff, N., and Vuillot, F., "Numerical Simulations of Parietal Vortex-Shedding Phenomenon in a Cold-Flow Setup," AIAA Paper 98-3220, July 1998.

[38]Lupoglazoff, N., and Vuillot, F., "Parietal Vortex Shedding as a Cause of Instability for Long Solid Propellant Motors. Numerical Simulations and Comparisons with Firing Tests," AIAA Paper 96-0761, Jan. 1996.

[39]Lupoglazoff, N., and Vuillot, F., "Numerical Simulation of Vortex Shedding Phenomenon in Two-Dimensional Test Case Solid Rocket Motors," AIAA Paper 92-0776, Jan. 1992.

[40]Prevost, M., Vuillot, F., and Traineau, J. C., "Vortex-Shedding Driven Oscillations in Subscale Motors for the Ariane 5 MPS Solid Rocket Motors," AIAA Paper 96-3247, 1996.

[41]Flandro, G. A., "Solid Propellant Acoustic Admittance Corrections," *Journal of Sound and Vibration*, Vol. 36, No. 3, 1974, pp. 297–312.

[42]Flandro, G. A., "Effects of Vorticity Transport on Axial Acoustic Waves in a Solid Propellant Rocket Chamber," *Combustion Instabilities Driven by Thermo-Chemical Acoustic Sources*, NCA Vol. 4, HTD Vol. 128, American Society of Mechanical Engineers, New York, 1989, pp. 53–61.

[43]Majdalani, J., and Van Moorhem, W. K., "The Unsteady Boundary Layer in Solid Rocket Motors," AIAA Paper 95-2731, July 1995.

[44]Majdalani, J., and Van Moorhem, W. K., "A Multiple-Scales Solution to the Acoustic Boundary Layer in Solid Rocket Motors," *Journal of Propulsion and Power*, Vol. 13, No. 2, 1997, pp. 186–193.

[45]Majdalani, J., and Van Moorhem, W. K., "Improved Time-Dependent Flowfield Solution for Solid Rocket Motors," *AIAA Journal*, Vol. 36, No. 2, 1998, pp. 241–248.

[46]Culick, F. E. C., "The Stability of One-Dimensional Motions in a Rocket Motor," *Combustion Science and Technology*, Vol. 7, No. 4, 1973, pp. 165–175.

[47]Barron, J., Majdalani, J., and Van Moorhem, W. K., "A Novel Investigation of the Oscillatory Field over a Transpiring Surface," *Journal of Sound and Vibration*, Vol. 235, No. 2, 2000, pp. 281–297.

[48]Brown, R. S., Blackner, A. M., Willoughby, P. G., and Dunlap, R., "Coupling between Velocity Oscillations and Solid Propellant Combustion," Final TR F49620-81-C-0027, Bolling AFB, Washington, DC, Aug. 1986.

[49]Dunlap, R., Blackner, A. M., Waugh, R. C., Brown, R. S., and Willoughby, P. G., "Internal Flowfield Studies in a Simulated Cylindrical Port Rocket Chamber," *Journal of Propulsion and Power*, Vol. 6, No. 6, 1990, pp. 690–704.

[50]Majdalani, J., "Boundary-Layer Structure in Cylindrical Rocket Motors," *AIAA Journal*, Vol. 37, No. 4, 1999, pp. 505–508.

[51]Majdalani, J., and Roh, T. S., "The Oscillatory Channel Flow with Large Wall Injection," *Proceedings of the Royal Society, Series A: Mathematical and Physical Sciences*, Vol. 456, No. 1999, 2000, pp. 1625–1657.

[52]Majdalani, J., "The Oscillatory Channel Flow with Arbitrary Wall Injection," *Journal of Applied Mathematics and Physics*, Vol. 52, No. 1, 2001, pp. 33–61.

[53]Majdalani, J., and Van Moorhem, W. K., "Laminar Cold-Flow Model for the Internal Gas Dynamics of a Slab Rocket Motor," *Journal of Aerospace Science and Technology*, Vol. 5, No. 3, 2001, pp. 193–207.

[54]Majdalani, J., and Flandro, G. A., "The Oscillatory Pipe Flow with Arbitrary Wall Injection," *Proceedings of the Royal Society, Series A: Mathematical and Physical Sciences*, Vol. 458, No. 2022, 2002, pp. 1–31.

[55]Yuan, S. W., "Further Investigation of Laminar Flow in Channels with Porous Walls," *Journal of Applied Physics*, Vol. 27, No. 3, 1956, pp. 267–269.

[56]Venugopal, P., Najjar, F. M., and Moser, R. D., "Numerical Simulations of Model Solid Rocket Motor Flows," AIAA Paper 2001-3950, July 2001.

[57]Apte, S., and Yang, V., "Effect of Acoustic Oscillation on Flow Development in a Simulated Nozzleless Rocket Motor," *Solid Propellant Chemistry, Combustion, and Motor Interior Ballistics*, edited by V. Yang, T. B. Brill, and W.-Z. Ren, Vol. 185, Progress in Astronautics and Aeronautics, AIAA, Reston, VA, 2000, pp. 791–822.

[58]Zhou, C., and Majdalani, J., "Improved Mean Flow Solution for Slab Rocket Motor with Regressing Walls," AIAA Paper 2000-3191, July 2000.

[59]Goto, M., and Uchida, S., "Unsteady Flows in a Semi-Infinite Expanding Pipe with Injection through Wall," *Transactions of the Japan Society for Aeronautical and Space Sciences*, Vol. 33, No. 9, 1990, pp. 14–27.

[60]Proudman, I., and Johnson, K., "Boundary-Layer Growth near a Rear Stagnation Point," *Journal of Fluid Mechanics*, Vol. 12, 1962, pp. 161–168.

[61]Yuan, S. W., and Finkelstein, A. B., "Laminar Pipe Flow with Injection and Suction Through a Porous Wall," *Journal of Applied Mechanics, Series E*, Vol. 78, May 1956, pp. 719–724.

[62]Ma, Y., Van Moorhem, W. K., and Shorthill, R. W., "Innovative Method of Investigating the Role of Turbulence in the Velocity Coupling Phenomenon," *Journal of Vibration and Acoustics*, Vol. 112, No. 4, 1990, pp. 550–555.

[63]Ma, Y., Van Moorhem, W. K., and Shorthill, R. W., "Experimental Investigation of Velocity Coupling in Combustion Instability," *Journal of Propulsion and Power*, Vol. 7, No. 5, 1991, pp. 692–699.

[64]Sutton, G. P., *Rocket Propulsion Elements*, 6th ed., Wiley, New York, 1992, pp. 370, 375, 418, 435.

[65]Reid, R. C., Prausnitz, J. M., and Poling, B. E., *The Properties of Gases and Liquids*, 4th ed., McGraw–Hill, New York, 1987, pp. 388–490.

[66]Beckstead, M., "Overview of Combustion Mechanisms and Flame Structures for Advanced Solid Propellants," *Solid Propellant Chemistry, Combustion, and Motor Interior Ballistics*, edited by V. Yang, T. B. Brill, and W.-Z. Ren, Vol. 185, Progress in Astronautics and Aeronautics, AIAA, Reston, VA, 2000, pp. 267–285.

[67]Uchida, S., and Aoki, H., "Unsteady Flows in a Semi-Infinite Contracting or Expanding Pipe," *Journal of Fluid Mechanics*, Vol. 82, No. 2, 1977, pp. 371–387.

[68]Terrill, R. M., "On Some Exponentially Small Terms Arising in Flow through a Porous Pipe," *Quarterly Journal of Mechanics and Applied Mathematics*, Vol. 26, No. 3, 1973, pp. 347–354.

S. K. Aggarwal
Associate Editor